Self-consistent computation of X-ray mirror Point Spread Functions from surface profile and roughness

L.Raimondi[1,2] and D.Spiga[2]

[1]Universitá degli Studi dell'Insubria, via Ravasi, 2, I-21100, Varese (VA), Italy;
[2]INAF/ Osservatorio Astronomico di Brera, Via E. Bianchi 46, I-23807 Merate (LC), Italy

ABSTRACT

The angular resolution degradation of an X-ray mirror, represented by its Point Spread Function (PSF), is usually simulated accounting for geometrical deformations and microroughness of its surface. When the surface profile is analyzed in terms of Fourier components, figure errors comprise the spectral regime of long spatial wavelengths, whilst microroughness falls in the regime of high spatial frequencies. The first effect is in general simulated along with geometrical optics, while the second contribution - that heavily depends on the energy of X-rays - is derived from the known scattering theory, i.e., from physical optics. A drawback of this method, indeed, is that the separation between the geometrical and physical optics regime is not abrupt. Moreover, it is not clear how one should merge the PSFs derived from the two computations to retrieve an affordable reconstruction of the PSF of the mirror. In this paper we suggest a method to compute the mirror PSF from longitudinal profiles of a grazing incidence mirror, based uniquely on physical optics. The treatment makes use of Fresnel diffraction from measured profiles or simulated from the PSD (Power-Spectral-Density) of surface roughness. Even though this approach was already adopted in the past to simulate the sole X-ray scattering, in this work we show, along a series of simulations, that it can be applied to reproduce the effect of scattering, aperture diffraction and figure errors as well. The computation returns the PSF at any X-ray energy, it is self-consistent and does not require setting any boundary between figure errors and roughness.

Keywords: X-ray mirrors, Point Spread Function, figure errors, X-ray scattering

1. INTRODUCTION

The angular resolution of an imaging X-ray telescope is chiefly determined by the optical quality of its focusing optics. These in general consist of a variable number of nested grazing-incidence, double-reflection X-ray mirrors. A widespread mirror profile is usually the Wolter-I (parabola+hyperbola[1]), even though polynomial[2] or Kirkpatrick-Baez[3] geometries are also suitable. The real optical performances of X-ray mirrors, indeed, are always worse than predicted by the mentioned designs, obviously due to mirrors imperfections. The mirror profile can be deformed at any production stage: manufacturing, integration, and handling. Similarly, the mirror surface is not ideally smooth but characterized by a rough topography, as it can be observed along with optical interferometers or Atomic Force Microscopes. Both kind of imperfections concur to determine an optical imaging degradation: a common way to describe the optical performance is its *Half Energy Width* (HEW), even a more complete information on the radial distribution of focused photons is provided by the *Point Spread Function* (PSF), i.e., the annular integral of the focused X-ray intensity around the center of the focal spot. The HEW is twice the median value of the PSF. A basic issue in X-ray optics is to establish a relation between the mirror imperfections and its PSF – or the HEW – as a function of the X-ray energy, in order to i) predict the angular resolution of the optics from measured profiles and roughness, and ii) establish the tolerable level of mirror imperfections from the desired angular resolution.

Apart from definitions related to the measurement technique, or empirically referred to the mirror length,[4] the separation of the two mentioned sources of degradation of the PSF, profile geometry and roughness, reflect in general the different kind of treatment performed to predict their effect on the angular resolution. Profile errors are believed to fall in the *geometrical optics* regime, therefore they are analyzed along with ray-tracing routines since the path of each X-ray, and in particular the reflection point on the mirror surface, is assumed to be uniquely reconstructed. In contrast, the surface roughness is assumed to entirely fall in a spectral region of Fourier surface wavelengths where the concept of "ray" is no longer applicable, because the optical path differences involved begin to be comparable with λ, the X-ray wavelength. The imaging degradation is due, in this spectral range, to the X-ray scattering (XRS), i.e., the off-surface diffraction of the reflected X-ray wavefront, and a well-established first order theory is available[5] to compute the scattering diagram from the power spectrum of the roughness, or its *Power Spectral Density*[6] (PSD).

Even though several contributions[7,8,9,10] were given in the past years in order to establish a relationship between the mirror PSF and the surface finishing level, all these approaches require treating separately the geometrical profile and the roughness effects. This in turn requires one to set a spatial frequency that serves as a boundary between the two regimes, which presumably depends on the incidence angle θ_i and λ. However, this limiting frequency is neither abrupt, nor clearly established, therefore the adoption of the geometric or scattering treatment has so far been, within large limits, "a matter of taste".[11] To make things worse, even if such a limit were clearly set, the mentioned X-ray scattering theory is valid only within the *smooth surface limit*, i.e., on condition that

$$4\pi\sigma\sin\theta_\mathrm{i} < \lambda, \tag{1}$$

where θ_i is the grazing incidence angle of X-rays and σ is its surface rms in a given spectral band. As a consequence, the first order theory cannot be always extended to the low-frequency limit, where the surface defects are expectedly higher.

Some light in identifying the separation between the spectral ranges of figure errors and roughness was shed by Aschenbach,[11] who concluded that a *single* Fourier component whose rms fulfills the smooth-surface condition (Eq. 1) should be mostly treated as roughness, and as figure error otherwise. However, the criterion operates a selection on the rms values of a spectrum of *discrete* frequencies, therefore it appears difficult to apply to a continuous roughness spectrum since the "single component" rms would depend on the spectral resolution adopted, which in principle can be made as small as one wants.

A different approach to the problem of translating the HEW scattering term of a mirror, as a function of the X-ray energy, into a surface finishing requirement, was elaborated in 2007 by one of us.[12] This method, based on the first order scattering theory, yielded analytical formulae that can be used to convert the surface PSD of a mirror – with an arbitrary number of identical reflections – into the X-ray scattering term of the HEW, as a function of λ, and vice versa. Although the method is fast and reliable, it still suffers from the assumption that a separation between figure errors and roughness treatment can be uniquely set. Moreover, it requires the surface PSD in use to entirely fall in the smooth surface limit, and finally, the computed XRS term of the HEW is *assumed* to be small and added quadratically to the figure error HEW, an assumption difficult to verify immediately.

A pathway to get around these problems was suggested in 2003 by Zhao and van Speybroeck,[13] who treated the XRS as surface diffraction in Fraunhofer approximation to overcome the smooth surface and small scattering angle limits. Nevertheless, they seem to have restricted this method to the sole XRS computation. In this paper we generalize their method, by showing that we can predict the PSF – and consequently the HEW – of a single, grazing incidence parabolic X-ray mirror from measured or simulated longitudinal profiles, simply making use of the Fresnel diffraction theory. This is a widespread technique to compute the PSF in the UV or visible light to account for the diffraction aperture and optical aberrations, but apparently it seems not to have been applied to rough mirror profiles, i.e., accounting for both profile errors and roughness in a *very wide spectral range of frequencies.* We show that if this is done, the mirror PSF can be computed *from UV to hard X-rays* without relevant approximations but that we neglect mirror roundness errors, since in grazing incidence they have a lesser impact on the PSF.

Another advantage of this method is that it is self-consistent: one does not need to adopt different treatments in different spectral ranges. The geometrical optics results are automatically obtained at X-ray energies at which aperture diffraction and X-ray scattering turn out to be negligible *a posteriori.* Whenever such energy ranges can be identified, we are allowed to define a "figure error" HEW term, and therefore we can compare of the computed HEW(λ) from Fresnel diffraction with the results obtained from the analytical treatment[12] of the XRS term of the HEW. A very good agreement is found for the 2 considered cases, provided that the two terms of the HEW are summed linearly, rather than in quadrature as initially supposed. The results are briefly discussed in the last section.

2. POINT SPREAD FUNCTION CONSTRUCTION METHODOLOGY

In this approach, we construct the PSF of the mirror using the Huygens-Fresnel principle. The grazing incidence allows us to adopt some very reasonable approximations: the first one is that we can compute in scalar approximation: secondly, we can use for computation the meridional *profiles* rather than the complete mirror map, ignoring thereby the surface defects in the azimuthal direction. The last approximation, which allows dramatically reducing the computational complexity and time, is justified by the following considerations:

1. The *X-ray scattering* pattern in grazing incidence is 100 to 1000 times more extended in the incidence plane than in the perpendicular direction, i.e., it essentially lies in the incidence plane.[5] Moreover, it is determined by the roughness PSD as computed in incidence plane direction; therefore it is unaffected by the profiles along the azimuth.

2. If the geometrical optics is applicable, the slope errors of the longitudinal sections of the mirror result in an angular dispersion twice as large, while the same slope errors along the azimuth result in an angular spread of rays smaller by a factor of $\tan 2\alpha$, where α is the incidence angle. Therefore, the deviation of reflected rays is dominated by the slope variation of the longitudinal sections.

3. Finally, if α is small enough, the mirror aperture is a thin circular corona, whose width is much smaller than the mirror radius. In these conditions also the *aperture diffraction* – visible when testing the mirror PSF in UV light – resembles the diffraction pattern of a long, straight slit, which can be computed monodimensionally. This can be seen from Fig. 1, where we compare the aperture diffraction PSF of a thin circular corona aperture and the one of a straight slit of the same width.

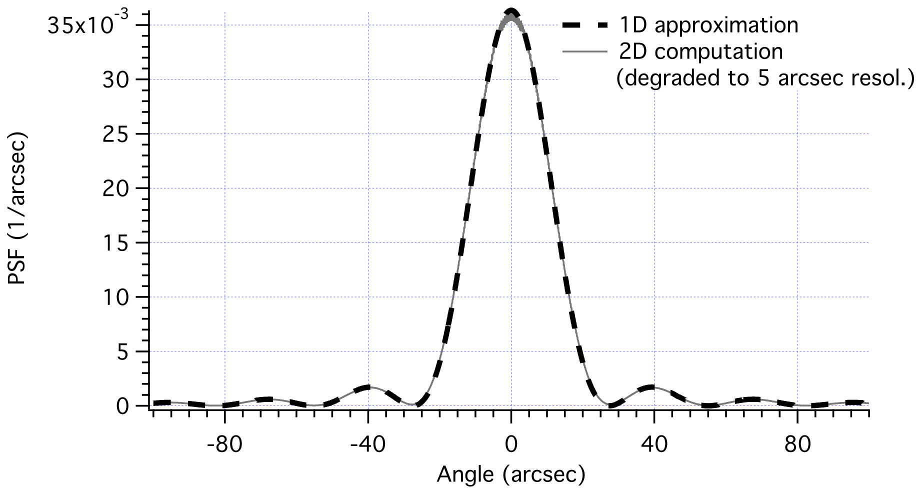

Figure 1. The aperture diffraction PSF at $\lambda = 3000$ Å of a grazing incidence parabolic mirror with $f = 10$ m, a minimum radius $R_0 = 150$ mm, and a length $L = 300$ mm, resulting in a circular corona aperture of 2.25 mm width. The dashed line is the usual diffraction pattern of a straight slit 2.25 mm wide, while the accurate computation (solid line) is obtained computing the exact diffraction pattern integrated over circular coronae. The first pattern would exhibit a superimposed high-frequency modulation, but it is smoothed out by the finite resolution of the detector (5 arcsec).

In this work, we limit ourselves to the PSF computation for a single-reflection mirror with a parabolic nominal profile. We define (see Fig. 2) f to be the focal length of the mirror, R_0 and R_M its minimum and maximum radii, L its length along the z-axis. We define the radial aperture $\Delta R = R_\mathrm{M} - R_0 \approx L \tan\alpha$. The focal plane section along which the PSF is evaluated is the x-axis. We initially consider the case of a perfectly parabolic profile, which is expected to return a delta-like PSF. We treat later the real cases of mirrors with deformations and with a rough surface, whose PSF is expectedly broader, by applying the same computation to the actual profile. In any case, the generic mirror profile, $z_p(x_p)$, act as a diffractor of a electromagnetic plane wave of wavelength λ and electric field amplitude E_0, initially oriented in the negative direction of the z-axis. The superpositions on the focal plane of the secondary waves generated at each point of the mirror returns the total electric field, neglecting the obliquity factor,

$$E(x,y) = \int_S \frac{E_0}{d_2\lambda} \exp\left[-2i\pi \frac{d_1+d_2}{\lambda}\right] \mathrm{d}^2 s, \tag{2}$$

where d_1 and d_2 are the distance of the generic mirror point from the initial wavefront, and from the focal plane point at x, respectively. The integral is meant to be extended to a "slice" , S, of the mirror with the actual longitudinal profile and a small width Δy along the azimuth. Because $f \gg L$, we are allowed to approximate $d_2 \approx f$ in the denominator of Eq. 2.

The two distances can be written, to a very good approximation, as

$$d_1 = L + f - z_p, \tag{3}$$

and

$$d_2 = \sqrt{(x-x_p)^2 + y_p^2 + z_p^2} \approx \sqrt{(x-x_p)^2 + z_p^2} + \frac{y_p^2}{2f}. \tag{4}$$

By noting that the mirror curvature along the azimuth focuses the rays in the y direction, the last term has to be written[14] as $y_p y/f$ in Fraunhofer approximation, and the Eq. 2 becomes

$$E(x,y) = \frac{E_0}{f\lambda} \int_L e^{-i\frac{2\pi}{\lambda}(L+f-z_p+\sqrt{(x-x_p)^2+z_p^2})}\, \mathrm{d}l \int_{-\Delta y/2}^{+\Delta y/2} e^{-i\frac{\pi y}{\lambda f} y_p}\, \mathrm{d}y_p. \tag{5}$$

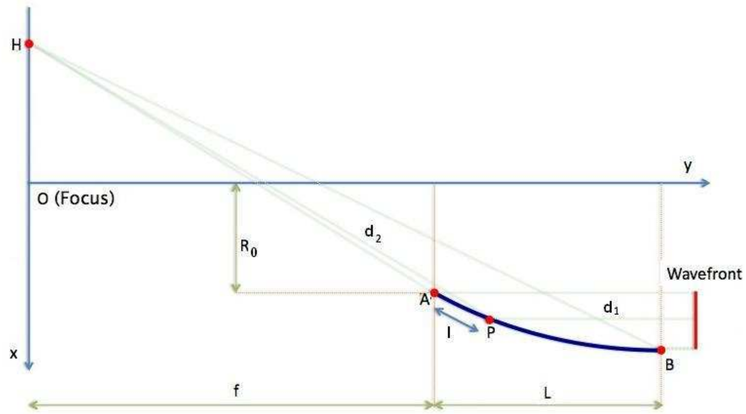

Figure 2. The adopted geometry for the computation of the PSF of a parabolic mirror. A plane wavefront impinges the mirror from right side, and the scattered amplitude at the generic point H of the focal plane is obtained by superposing the secondary waves generated at each point of the mirror profile, P, located along the curvilinear abscissa l.

The second factor in the Eq. 5 can be integrated easily, and we remain with

$$E(x) = \frac{E_0}{f\lambda} \int_L e^{-i\frac{2\pi}{\lambda}(L+f-z_p+\sqrt{(x-x_p)^2+z_p^2})}\, \mathrm{d}l\, \Delta y \frac{\sin\delta}{\delta}, \tag{6}$$

where $\delta = \frac{\pi y \Delta y}{\lambda f}$. The intensity distribution then becomes

$$I(x,y) = \frac{E_0^2}{f^2\lambda^2} \left| \int_L e^{-i\frac{2\pi}{\lambda}(\sqrt{(x-x_p)^2+z_p^2}-z_p)}\, \mathrm{d}l \right|^2 (\Delta y)^2 \frac{\sin^2\delta}{\delta^2}. \tag{7}$$

To obtain the distribution along the x-axis, we integrate the intensity distribution along y. However, since $\lambda \ll \Delta y$, the last factor becomes a Dirac delta; therefore the integral on y is immediate and we obtain

$$I(x) = \frac{E_0^2\,\Delta y}{f\lambda} \left| \int_L e^{-i\frac{2\pi}{\lambda}(\sqrt{(x-x_p)^2+z_p^2}-z_p)}\, \mathrm{d}l \right|^2 : \tag{8}$$

this is the intensity profile along the x-axis, but it is the PSF of the mirror as well, because the entire intensity distribution on the focal plane is obtained by superposing the linear diffraction from every "slice" in its meridional plane. The mirror curvature in the azimuth causes the diffracted intensity (Eq. 8) to be spread over an increasing surface with the angular distance from the focus, but this spread is compensated by the integration over the circular coronae. Finally, we normalize the PSF to the total power impinging the mirror, $\Delta R \Delta y E_0^2$, and we obtain the final formula

$$PSF(x) = \frac{1}{f\lambda\,\Delta R}\left|\int_L e^{-i\frac{2\pi}{\lambda}\left(\sqrt{(x-x_p)^2+z_p^2}-z_p\right)}\,\mathrm{d}l\right|^2. \tag{9}$$

This is the equation we will use throughout the remainder of this paper.

The integral in Eq. 9 can be computed numerically for *any* profile of the mirror, $z_p(x_p)$, at *any* X-ray wavelength, to compute the mirror PSF that simultaneously account for aperture diffraction, figure errors and X-ray scattering without setting any boundary between the different regimes. We only have to determine the minimum profile sampling at which the integral has to be computed to avoid the appearance of aliases: we can do it by noting that, if the focal plane has a half-width r, the maximum scattering angle is r/f, therefore for a wavelength λ the minimum spatial wavelength scattering at the focal plane's edge is, using the grating formula,

$$l_{\min} \approx \frac{\lambda f}{r \sin\alpha}. \tag{10}$$

In a conservative approach, we will hereafter oversample the minimum wavelength by a 2π factor:

$$\Delta l \approx \frac{\lambda f^2}{\pi R_0 r}, \tag{11}$$

where we made use of the relation $R_0 \simeq f\sin(2\alpha)$, for a single-refection mirror. We consider hereafter the test case of a mirror with reasonable parameters, $R_0 = 150$ mm, $L = 300$ mm, and $f = 10$ m, yielding $\alpha \simeq 0.42$ deg. The focal plane is assumed to be 2 cm wide. In hard X-rays we admit that $\lambda > 0.1$ Å, so we obtain a sampling step $\Delta l > 0.2$ μm, corresponding to a sum of 10^6 terms per profile at most.

3. EXAMPLES OF COMPUTATION OF POINT SPREAD FUNCTIONS

In this section we show some applications of Eq. 9 to derive the PSF of a parabolic X-ray mirror with different profile errors. We consider first the theoretical case of a perfect parabolic mirror, whose PSF is solely affected by the aperture diffraction. In the following section we check the behaviour of a single frequency perturbation superimposed to the mirror profile. Finally, we simulate a realistic case of a mirror with a geometrical deformation and a microroughness relief.

3.1 The PSF of ideally smooth mirrors

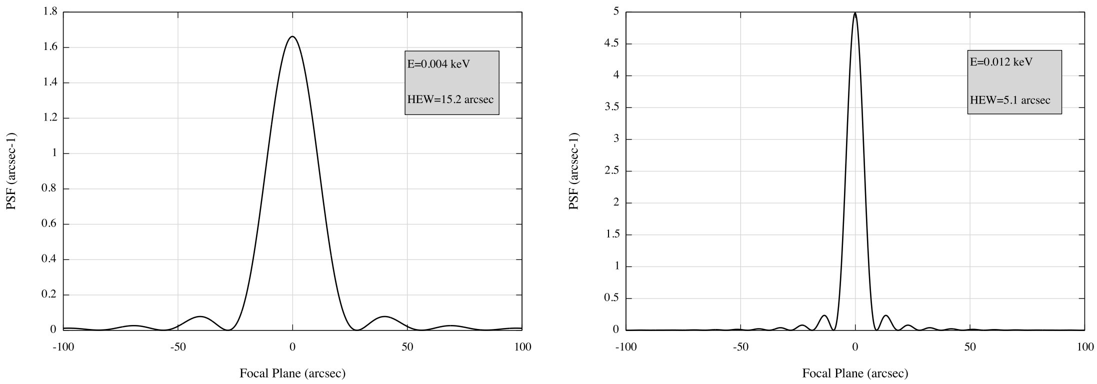

Figure 3. The PSF of an ideal parabolic mirror at 3000 Å (left) and 1000 Å (right).

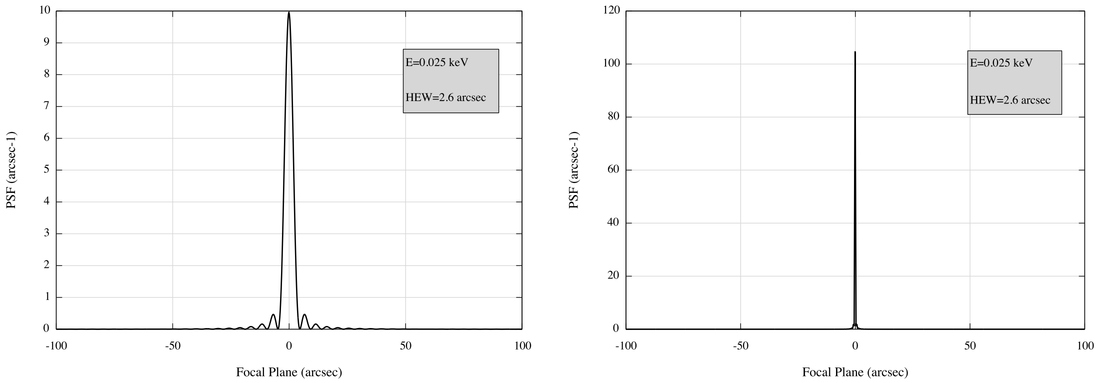

Figure 4. The PSF of an ideal parabolic mirror at 500 Å (left) and 30 Å (right). Almost no change is visible beyond this wavelength.

Adopting a parabolic profile $z_p = z_p(x_p)$ and solving Eq. 9, we have computed the PSF from 3000 Å to 30 Å. We expect that the effect of diffraction aperture is dominant in the UV, while the PSF approaches a Dirac delta as the energy is increased. The computation behaves as expected. In Fig. 3 we display the PSF at 3000 Å and 1000 Å, completely enlarged by the aperture diffraction. As the X-ray energy is increased, the aperture diffraction decreases and the PSF tends to resemble a Dirac delta (Fig. 4).

3.2 Behavior of a sinusoidal perturbation

As a following example, we consider the case of a *single frequency* perturbation superimposed to the parabolic profile. In particular, we choose the spatial wavelength – ϕ =1 cm – and the amplitude – $A = 0.1$ μm – in a range that cannot be immediately classified as "figure error" or "microroughness", and therefore is usually labelled as "mid-frequency". We hereafter see that such a frequency can behave as roughness, figure error, or a mixture of the two, depending on λ. More precisely, as already derived by Aschenbach,[11] its behavior depends on whether λ exceeds or not the characteristic wavelength $4\pi\sigma \sin\alpha$, where α is the incidence angle and σ the rms of the sinusoid.

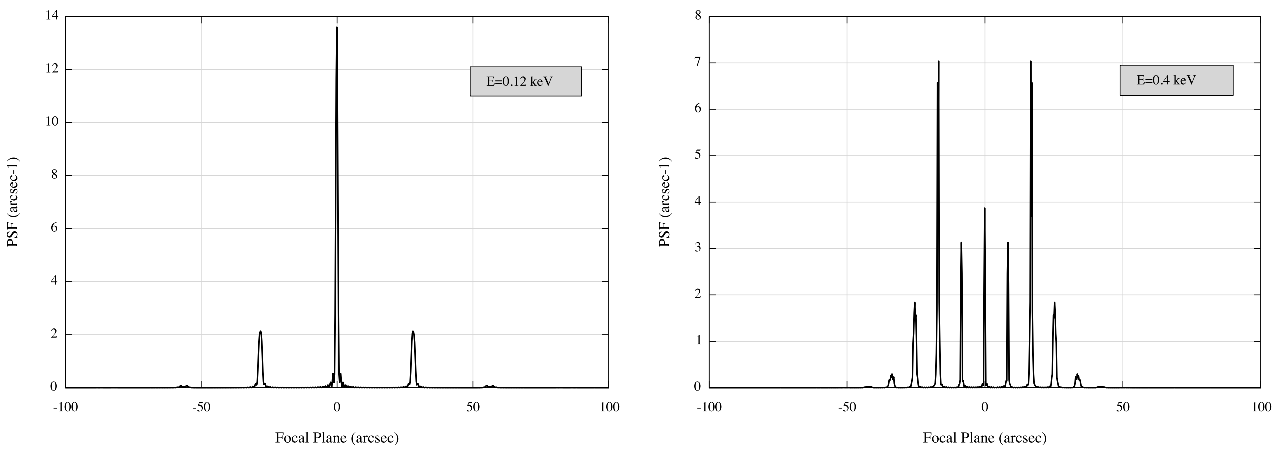

Figure 5. Computed PSF of a parabolic mirror plus a sinusoidal perturbation of 0.1 μm amplitude and a 1 cm period, for an X-ray wavelength of 100 Å (left) and 30 Å (right). The higher diffraction orders appear when the smooth-surface limit is no longer met.

As long as $\lambda \gg 4\pi\sigma \sin\alpha$, only the central spot of the PSF is visible. However, as λ is decreased, two peaks appear aside the focus, while the central peak decreases (Fig. 5, left). This situation is found when still $\lambda > 4\pi\sigma \sin\alpha$, but starts to be comparable. This is exactly, if fulfilled, the smooth-surface Rayleigh condition,[6] which allows us to apply the X-ray scattering theory at first order.[5] The two scattering peaks exactly correspond to the PSD peaks at the 1 cm frequency, for an X-ray energy of 0.04 keV and an incidence angle of 0.42 deg. However, if λ is decreased further, the situation changes because the scattering theory at the first order becomes no longer applicable: in Fig. 5 (right) we show the PSF computed at 30 Å, a wavelength *almost exactly at the boundary of the smooth-surface condition* (33 Å) for the considered example. We see that the higher scattering orders appear gradually, making the PSF more complex than predicted by the first order theory.

The mentioned example also allows us to check the correctness of our approach, because the peak positions and intensity are predicted by the sinusoidal grating theory:[6] more exactly, the scattering angles α_{s} fulfill the equation

$$\phi = \frac{N\lambda}{\cos\alpha - \cos\alpha_{\mathrm{s}}} \tag{12}$$

with N integer, and the N^{th} peak intensity is

$$I_N = J_N^2\left[\frac{2\pi A}{\lambda}(\sin\alpha + \sin\alpha_{\mathrm{s}})\right], \tag{13}$$

where J_N is the N^{th} Bessel function of the first kind. By means of Eqs. 12 and 13 we verified that the peak positions and heights of Fig. 5 match the theoretical predictions. This can be done at *any* X-ray energy: for instance, we can decrease λ below the limit $4\pi\sigma\sin\alpha$ and notice the evolution of the PSF: higher and higher diffraction orders appear then, until the peaks are superposed and cannot be easily discerned from each other. Despite that, we note that the PSF *does not expand*: rather, it tends to keep within definite angular limits ($\pm$ 26 arcsec in the present example, see Fig. 6, left), and when $\lambda \ll 4\pi\sigma\sin\alpha$, the PSF *tends to converge to a shape almost independent of* λ.

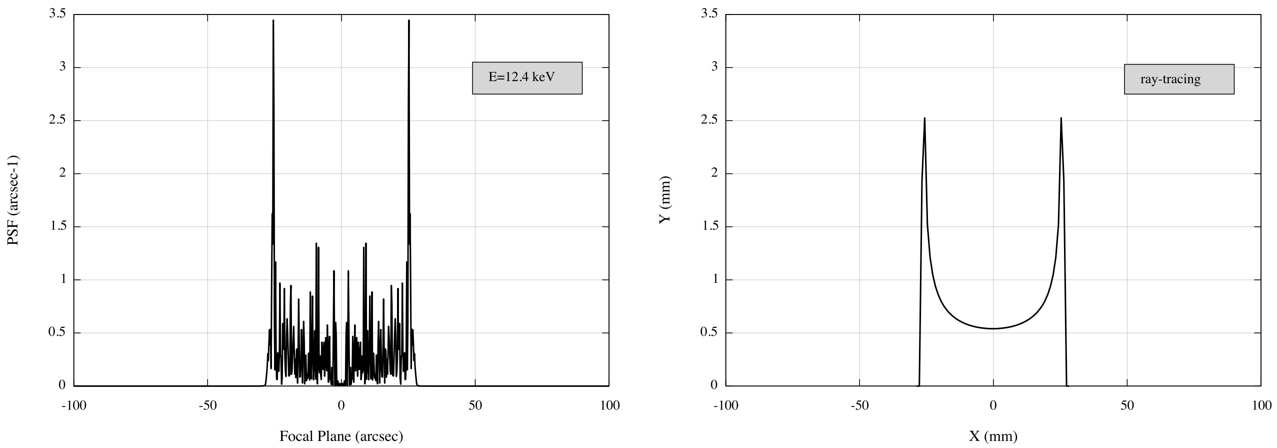

Figure 6. PSF computation of parabolic mirror plus a sinusoidal perturbation with $A = 0.1$ μm and $\phi = 1$ cm at $\lambda = 1$ Å (left). Ray-tracing simulation on the same sinusoidal profile (right), with the typical $1/\cos$ shape. The two PSFs differ only for the rapid modulation of the

The explanation of this behavior is the following: for very small λ values, the PSF is built up by high diffraction orders, and the intensity of diffraction peaks is given by Eq. 13. But for large N, $J_N(x)$ is nearly zero for $|x| < N$. Therefore, the PSF is non-zero if

$$\frac{2\pi A}{\lambda}(\sin\alpha + \sin\alpha_{\mathrm{s}}) > N. \tag{14}$$

By comparison with the Eq. 12, one obtains

$$\frac{2\pi A}{\phi}(\sin\alpha + \sin\alpha_{\mathrm{s}}) > \cos\alpha - \cos\alpha_{\mathrm{s}}, \tag{15}$$

which no longer depends on N and λ. For small angles, we can approximate $\sin\alpha \simeq \alpha$ and $\cos\alpha \simeq 1 - \alpha^2/2$, hence

$$\alpha_{\rm s}^2 - \alpha^2 < \frac{4\pi A}{\phi}(\alpha + \alpha_{\rm s}), \tag{16}$$

which is equivalent to

$$|\alpha_{\rm s} - \alpha| < \frac{4\pi A}{\phi} = 25.9\,\mathrm{arcsec}. \tag{17}$$

The limit on right hand of Eq. 17 is exactly the *twice the maximum slope of the sinusoidal perturbation*, corresponding to the maximum deviation of rays in geometrical optics approximation. We therefore find, as expected, that the application of the Fresnel diffraction for small λ returns the results of geometrical optics. This becomes even more apparent if we compare the PSF at 1 Å computed by Fresnel diffraction (Fig. 6, left) with the PSF computed by ray tracing on the same profile (Fig. 6, right). The two PSF essentially coincide, but for a rapid modulation of the PSF in the first case, which in practice is not observed due to the imperfect monochromaticity of real X-ray beams, which would cause the oscillations to be smoothed out. Summarizing, the method is able to reproduce in a self-consistent fashion the PSF of a" mid-frequency" deformation at any λ, regardless of whether it is considered "roughness" or "figure error". Obviously, in the limit of large λ, the PSF would be dominated by the aperture diffraction also in this case.

3.3 The PSF of rough mirrors: continuous power spectrum

The finished optical surface microrelief of X-ray mirrors cannot be obtained, in general, by superposing a discrete spectrum of frequencies (an exception is represented by mandrels at intermediate polishing stages, after the diamond turning process). Rather, their roughness is characterized by a *continuous* power spectral density, often modeled along with the power-law model,[15]

$$P(f) = \frac{K_n}{f^n}, \tag{18}$$

where $1 < n < 3$ and K_n is a factor representing numerically the PSD at 1 μm. After selecting reasonable values for the two parameters, we can construct infinite possible profiles corresponding to that PSD, from which we derive the PSF by means of Eq. 9. This situation would indeed correspond to the case of a rough but undeformed mirror. To account also for deformations that may arise at the manufacturing, integration, or handling stage, we superpose to the rough profile a deformation with a typical period equal to the mirror length. For the present simulation we adopt at all energies a 4$^{\rm th}$ order polynomial, 3 μm sag, long-period deformation (Fig. 7, left), superposed to rough profiles derived from Eq. 18 with either $n = 2.2$, $K_n = 0.5$ nm$^3\mu$m$^{-2.2}$ (Fig. 7, right). We have thereby computed the mirror PSF from UV to hard X-rays, applying Eq. 9. They are displayed, already with the correct normalizion, in Fig. 8 to 12.

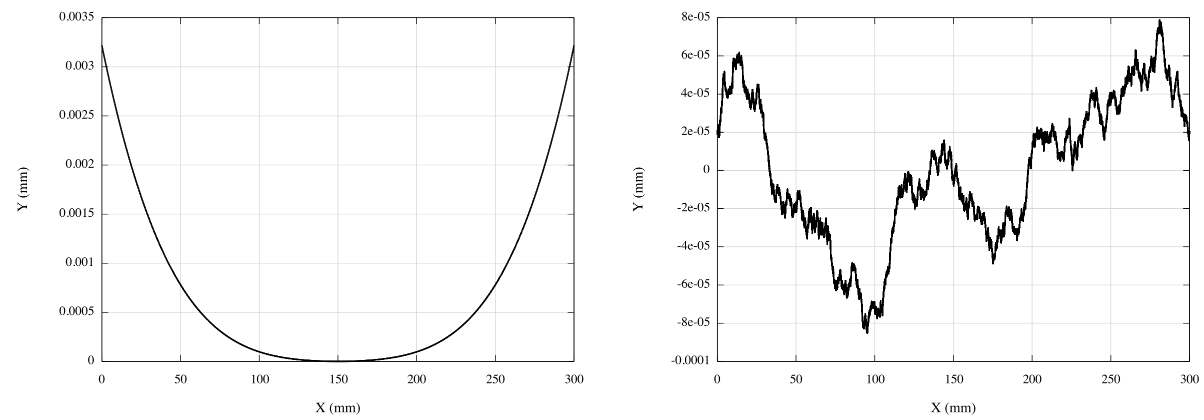

Figure 7. (left) the adopted "profile error" for this simulation and (right) a possible microroughness profile from a PSD with parameters $n = 2.2$ and $K_n = 0.5$ nm$^3\mu$m$^{-2.2}$.

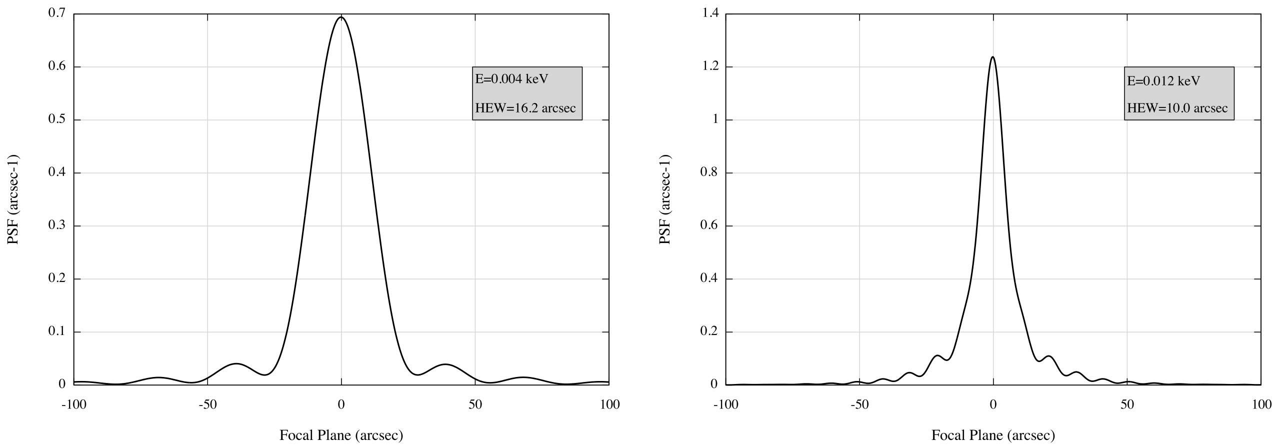

Figure 8. The simulated PSF in near UV, at (left) 3000 Å and (right) 1000 Å. The aperture diffraction prevails: the HEW is only slightly larger than for a perfect mirror (Fig. 3).

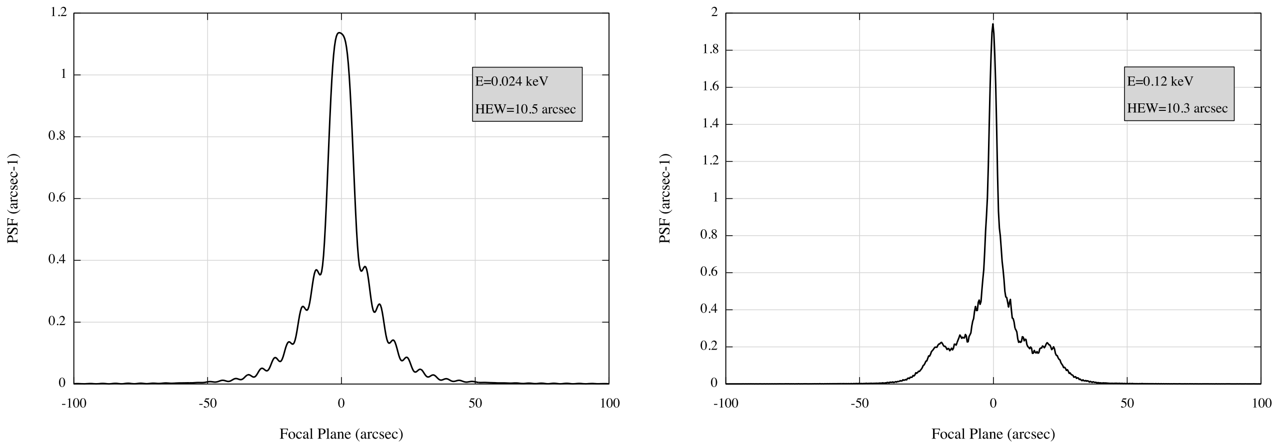

Figure 9. The simulated PSF in far UV, at (left) 500 Å and (right) 100 Å. The “figure errors” start to take over.

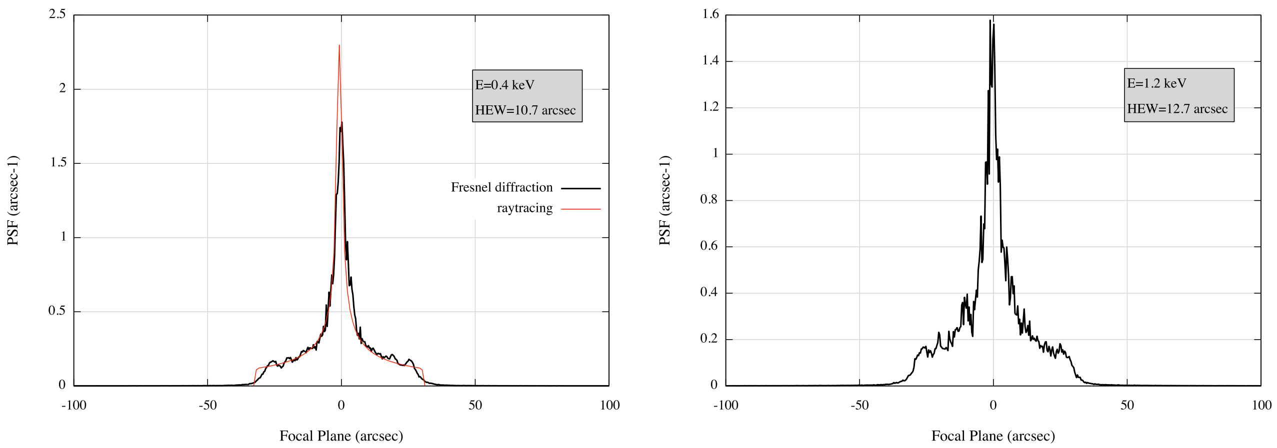

Figure 10. The simulated PSF in soft X-rays. At 30 Å(left), the PSF is dominated by mirror figure, since the PSF coincides with the ray-tracing of mirror with the polynomial deformation. At 10 Å(right), the X-ray scattering starts to appear, and the HEW begins to increase.

In UV light (Fig. 8) we can clearly see how the aperture diffraction component is dominant. Almost no effect of the deformation can be seen, and the roughness is completely irrelevant at these wavelengths. However, the diffraction peaks become less pronounced and the HEW diminishes as the energy is increased (Fig. 9), but it does not tend to a be infinitely narrow like in Sect. 3.1. At 100 Å, the PSF is already dominated by the polynomial deformation, with a 10 arcsec HEW, but it is around 0.4 keV (Fig. 10), that the geometrical optic is almost completely applicable, as the PSF can be computed by ray-tracing the mirror plus the sole polynomial profile. In X-rays (Fig. 11 and 12) the effect of roughness starts to be visible: the X-ray scattering causes the PSF to broaden, with a consequent HEW increase. For a more realistic simulation, the last 4 PSF's have been computed by averaging the results for 30 computations with different roughness profiles from the same PSD. This also allow to average out the PSF fringing, which in real cases is cancelled by the statistical nature of roughness.

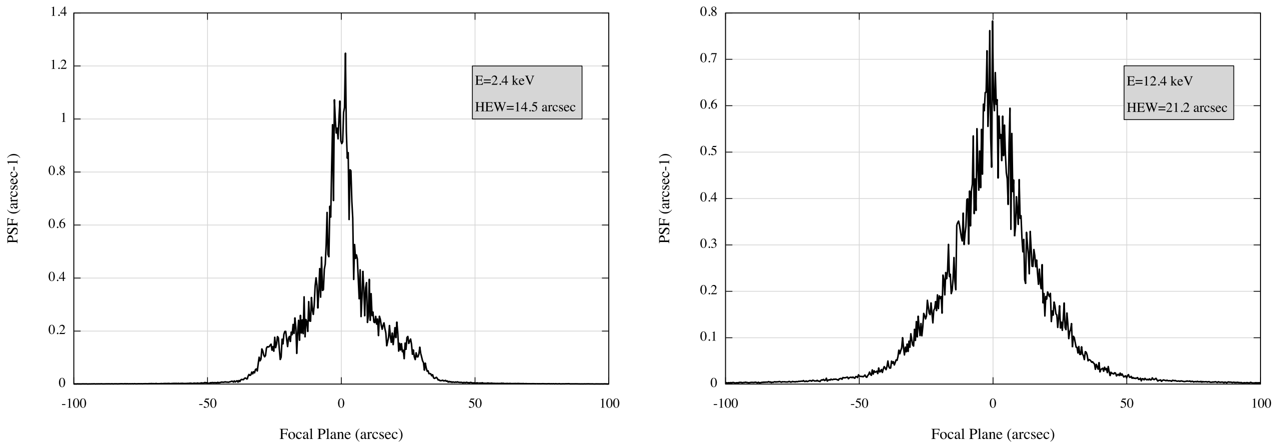

Figure 11. The simulated PSF in soft X-rays, at (left) 5 Å and (right) 1 Å. The X-ray scattering contribution is now clearly visible.

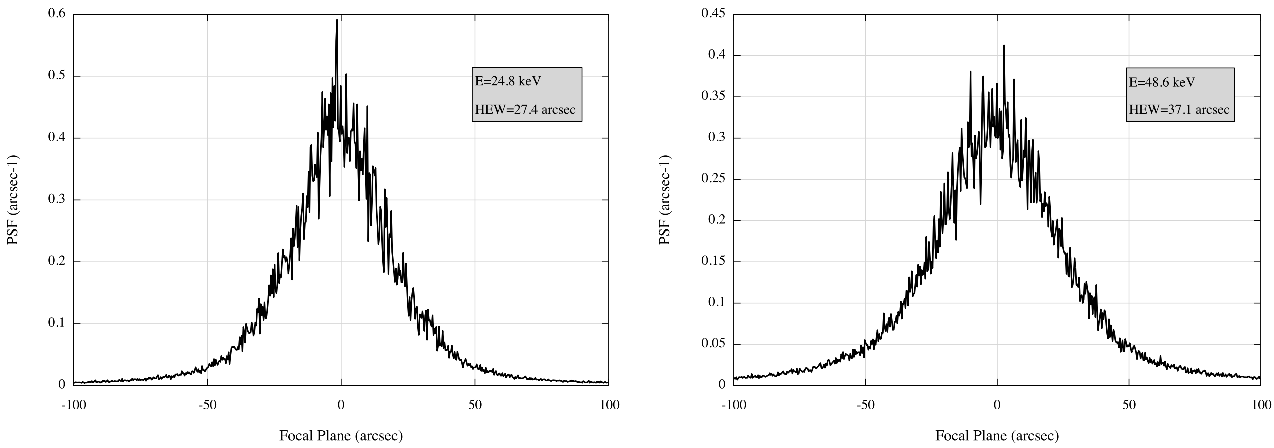

Figure 12. The simulated PSF in hard X-rays, at (left) 0.5 Å and (right) 0.25 Å. The X-ray scattering is now overwhelmingly dominating.

4. COMPARISON OF THE HEW RESULTS WITH THE ANALYTICAL MODEL

We finally compare the results of the PSF computation of Sect. 3.3 with the HEW predictions of the analytical model[12] mentioned in Sect. 1. To do that, we consider 2 possible couples of PSD parameters: either n = 2.2, K_n = 0.5 nm$^3\mu$m$^{-2.2}$, or n = 1.8, K_n = 2.2 nm$^3\mu$m$^{-1.8}$. Note that the first choice returns a steeper PSD, which has a larger content in low frequencies. This results in a different dependence of the HEW trend on the X-ray energy.

Firstly, we consider the case of a rough mirror without figure deformations. Form the PSF, computed using Eq. 9 at the X-ray energies, we have computed the HEW values as a function of the energy (Fig. 13, left) for the considered PSD. Then we compare them with the theoretical[12] scattering HEW prediction for a power-law PSD, in single reflection,

$$H(\lambda) = 2\left[\frac{16\pi^2 K_n}{(n-1)\ln 2}\right]^{\frac{1}{n-1}}\left(\frac{\sin\alpha}{\lambda}\right)^{\frac{3-n}{n-1}}. \tag{19}$$

Eq. 19 is a particular case of a more general formula[12] that allows computing the XRS term of the HEW from any PSD, and it can be applied because the PSD is below the smooth surface limit. The comparison shows a very good accord between the findings of the two techniques, excepting for the aperture diffraction, which cannot be reproduced by Eq. 19.

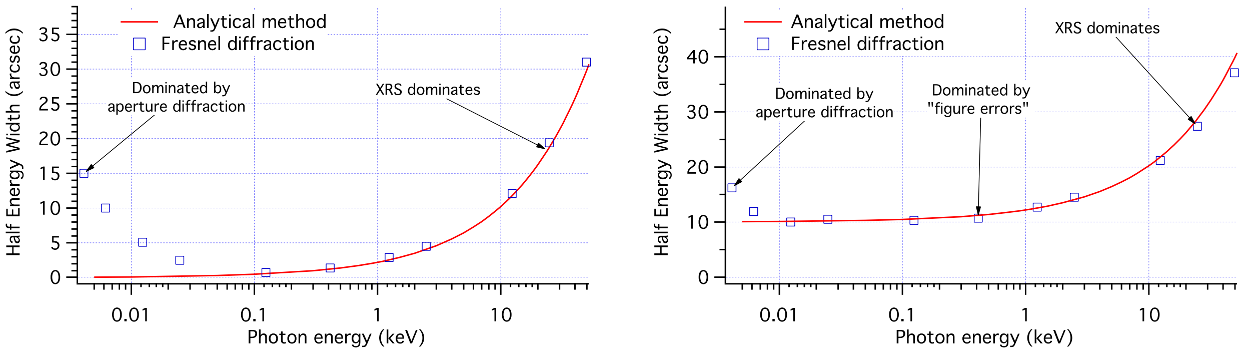

Figure 13. HEW simulations from the Fresnel diffraction and the analytical method: (left) roughness PSD only, with K_n = 0.5 nm$^3\mu$m$^{-2.2}$, n=2.2. (right) the same PSD, plus polynomial deformation.

As a second exercise we compare the HEW values with the analytical model, assuming not only a the mentioned PSD for roughness, but also the polynomial deformation. This is the case already treated in the previous section (Fig. 8 to 12). The results, in Fig. 13, right), are similar to the left panel, but the HEW in the region 0.01 – 1 keV is nearly constant and close to 10 arcsec. In this region we can therefore say that the PSF is dominated by "figure errors" because the HEW – which *a posteriori* we can denote as *figure HEW*, is almost independent of the X-ray energy and computable along with the geometrical optics. Interstingly, the Fresnel diffraction results can be reproduced by summing the figure HEW (10 arcsec) and Eq. 19 *linearly* instead of quadratically, as usually assumed. In Fig.14 we repeated the same exercise with the smoother power-law PSD: also in this case the agreement of the two methods is very good, even if the HEW trend diverges more steeply.

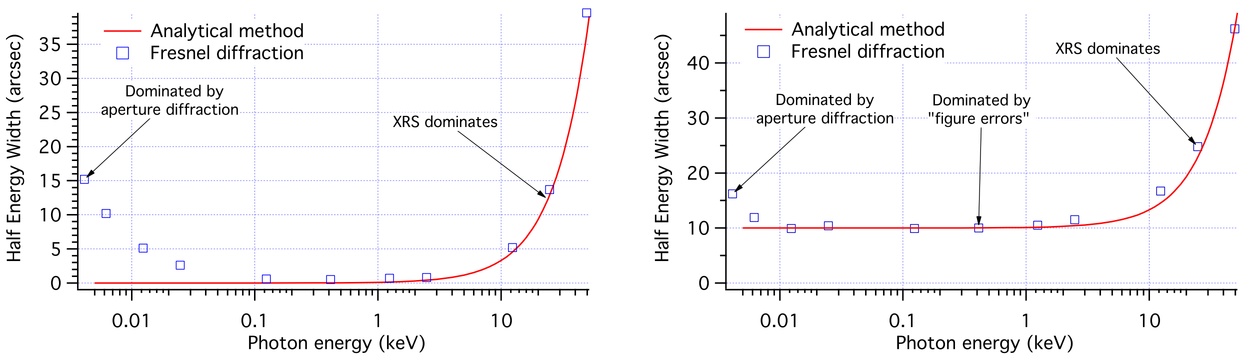

Figure 14. HEW simulations from the Fresnel diffraction and the analytical method: (left) roughness PSD only, with K_n = 2.2 nm$^3\mu$m$^{-1.8}$, n=1.8. (right) the same PSD, plus polynomial deformation.

5. CONCLUSIONS

In this work we have demonstrated how the Point Spread Function of a focusing X-ray mirror with imperfections can be computed at any monochromatic energy along with the Huygens-Fresnel principle, applied to meridional profiles of the mirrors. This can be done regardless of any distinction between figure errors and microroughness, also accounting for the aperture diffraction effects.

From this viewpoint, the classical distinction between figure errors and microroughness is unessential to the aim of computing the PSF: this treatment does not require setting any boundary. Moreover, the results of the geometrical optics and the first order scattering theory are automatically retrieved, wherever they can be applied, even if both represent asymptotical regimes not always well defined a priori. As an example, we have treated in a self-consistent way the behavior of a mid-frequency perturbation, in general difficult to manage because it cannot be uniquely attributed to one of two mentioned regimes. In particular, we have seen that the geometrical optics approximation results from the superposition of high order diffraction peaks, when their spacing becomes smaller than the detector spatial resolution.

ACKNOWLEDGMENTS

We thank P. Conconi (INAF/OAB) for useful discussions on the topics of aperture diffraction and ray-tracing.

REFERENCES

[1] L. P. Van Speybroeck, R. C. Chase, "Design parameters of paraboloid-hyperboloid telescopes for X-ray astronomy", Applied Optics, 11, 2, 440-445 (1972)

[2] P. Conconi, S. Campana, "Optimization of grazing incidence mirrors and its application to surveying X-ray telescopes", Astronomy & Astrophysics, 372, 1088-1094 (2001)

[3] P. Kirkpatrick, A. V. Baez, "Formation of optical images by x-rays", JOSA, 38, 766K (1948)

[4] P. A. J. De Korte, R. Giralt, J. N. Coste, et al., "EXOSAT X-ray imaging optics", Applied Optics, 20, 1080-1088 (1981)

[5] E. L. Church, H. A. Jenkinson, J. M. Zavada, "Relationship between surface scattering and microtopographic features", Optical Engineering, 18, 125-136 (1979)

[6] J. C. Stover, "Optical scattering: measurement and analysis", SPIE Optical Engineering Press (1995)

[7] F. E. Christensen, A. Hornstrup, H. W. Schnopper, "Surface correlation function analysis of high resolution scattering data from mirrored surfaces obtained using a triple-axis X-ray diffractometer", Applied Optics, 27, 1548-1563 (1988)

[8] J. E. Harvey, E. C. Moran, W. P. Zmech, "Transfer function characterization of grazing incidence optical systems", Applied Optics, 27, 1527-1533 (1988)

[9] R. Willingale, "ROSAT wide field camera mirrors", Applied Optics, 27, 1423-1439 (1988)

[10] S. L. O'Dell, R. F. Elsner, J. J. Kołodziejczak, et al., "X-ray evidence for particulate contamination on the AXAF VETA-1 mirrors", SPIE Proc. 1742, 171-182 (1993)

[11] B. Aschenbach, "Boundary between geometric and wave optical treatment of x-ray mirrors", SPIE Proc., 5900, 59000D (2005)

[12] D. Spiga, "Analytical evaluation of the X-ray scattering contribution to imaging degradation in grazing-incidence X-ray telescopes", Astronomy & Astrophysics 468, 775-784 (2007)

[13] P. Zhao, L. P. Van Speybroeck, 2003, "New method to model X-ray scattering from random rough surfaces". SPIE Proc. 4851, 124-139 (2003)

[14] A. L. Mieremet, M. W. Beijersbergen, "Fundamental spatial resolution of an x-ray pore optic". Applied Optics, 44(33) 7098-7105 (2005)

[15] E. L. Church, "Fractal Surface finish". Applied Optics, 27(8), 1518 -1526 (1988)